nature nanotechnology

Article

https://doi.org/10.1038/s41565-025-01885-5

Investigating the effect of heterogeneities across the electrode|multiphase polymer electrolyte interfaces in high-potential lithium batteries

Received: 23 November 2023

Accepted: 10 February 2025

Published online: 01 April 2025

Check for updates

Jungki Min[1,9], Seong-Min Bak[2,8,9], Yuxin Zhang[1], Mingyu Yuan[1], Nicholas F. Pietra[1,3], Joshua A. Russell[4], Zhifei Deng[5], Dawei Xia[1], Lei Tao[1], Yonghua Du[2], Hui Xiong[4], Ling Li[6], Louis A. Madsen[1,3] & Feng Lin[1,3,7]

Polymer electrolytes hold great promise for safe and high-energy batteries comprising solid or semi-solid electrolytes. Multiphase polymer electrolytes, consisting of mobile and rigid phases, exhibit fast ion conduction and desired mechanical properties. However, fundamental challenges exist in understanding and regulating interactions at the electrode|electrolyte interface, especially when using high-potential layered oxide active materials at the positive electrode. Here we demonstrate that depletion of the mobile conductive phase at the interface contributes to battery performance degradation. Molecular ionic composite electrolytes, composed of a rigid-rod ionic polymer with nanometric mobile cations and anions, serve as a multiphase platform to investigate the evolution of ion conductive domains at the interface. Chemical and structural characterizations enable the visualization of concentration heterogeneity and spatially resolve the interfacial chemical states over a statistically significant field of view for buried interfaces. We report that concentration and chemical heterogeneities prevail at electrode|electrolyte interfaces, leading to phase separation in polymer electrolytes. Understanding the hidden roles of interfacial chemomechanics in polymer electrolytes enables us to design an interphase tailoring strategy based on electrolyte additives to mitigate the interfacial heterogeneity and improve battery performance.

Solid-state batteries (SSBs) employing polymer electrolytes (PEs) can incorporate a lithium metal negative electrode, enabling a higher theoretical energy density compared with state-of-the-art graphite||lithium metal oxide Li-ion batteries using non-aqueous liquid electrolyte solutions[1–5]. PEs have received broad attention owing to their processibility, malleability and intimate conformability with the battery's electrodes[6]. Nevertheless, the wide application of PE-based SSBs is hampered by various interfacial issues, such as resistive surface layer formation, Li dendrite growth, formation of dead lithium (that is, metallic Li electrodepositions that are electrochemically inactive) and parasitic side reaction at electrode|electrolyte interfaces[7,8] (Fig. 1a). Unlike homogeneous PEs[9] (that is, ion transport is governed by segmental dynamics of the polymer host, such as in poly(ethylene oxide)), where ionic conductivity is reciprocally coupled to stiffness, multiphase PEs (that is, a combination of mobile phase for ion transport and rigid phase for mechanical support) can relax the coupling between these two

A full list of affiliations appears at the end of the paper. e-mail: fenglin@vt.edu

https://doi.org/10.1038/s41565-025-01885-5

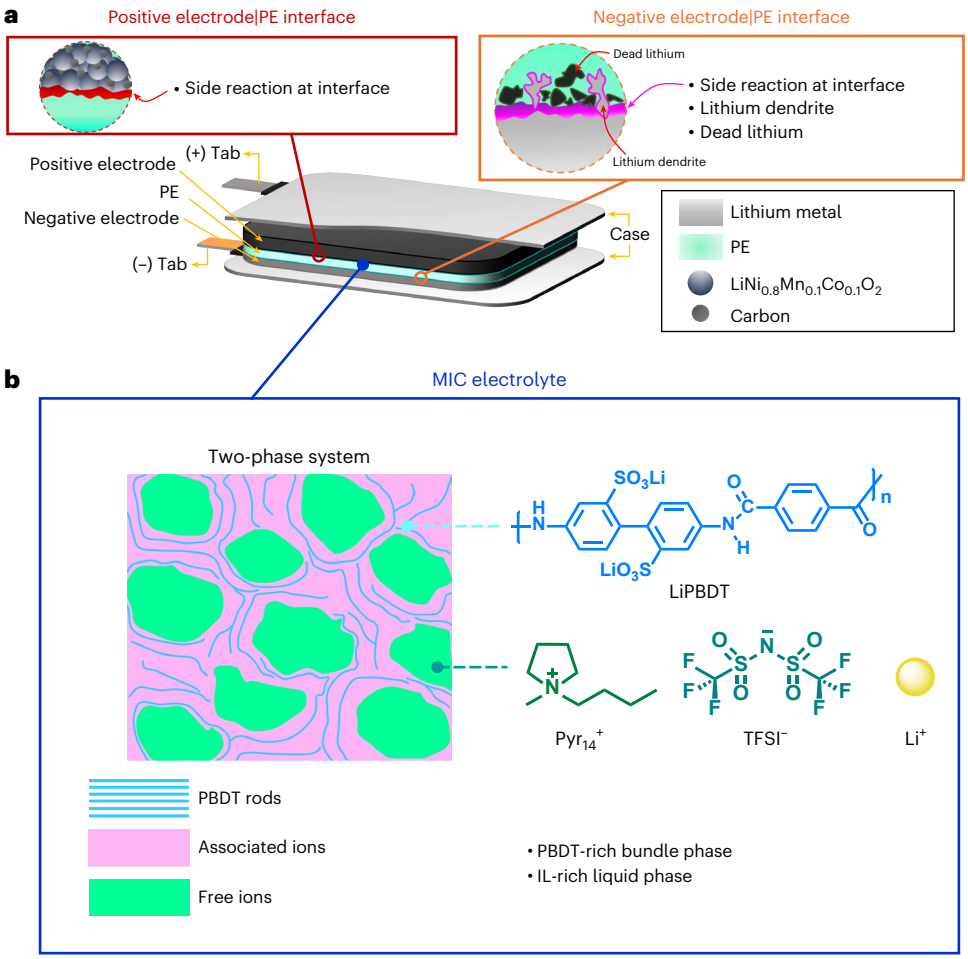

Fig. 1 | Graphic representation of interfaces and interphases in an Li metal pouch cell with an MIC electrolyte. a, Schematic representation of PE-based Li metal batteries and electrode|electrolyte mechanism involved therein. The interfacial side reaction at each electrode|electrolyte interface, dead lithium (electrochemically inactive Li metal deposits) and lithium dendrite from the negative electrode|electrolyte interface accelerates the interfacial degradation of the PE. $LiNi_{0.8}Mn_{0.1}Co_{0.1}O_2$ is the active material of the positive electrode, and carbon is used as a conductive agent. **b**, Schematic representation of the two-phase system in the MIC electrolyte. The bundles of poly-2,2′-disulfonyl-4,4′-benzidine terephthalamide (PBDT) double helix rods (blue lines) at a rod–rod distance of ~2 nm are held together with collective electrostatic (ion–ion) interactions (pink regions). The pink regions (PBDT-rich bundle phase) represent associated ions from IL and lithium salt (Pyr_{14}^+, $TFSI^-$ and Li^+) that are conjoined with bundles of PBDT double helix rods. The turquoise green regions (IL-rich liquid phase) represent free ions (Pyr_{14}^+, $TFSI^-$, and Li^+) similar to freely moving neat IL without PBDT rods. The two-phase system includes a co-continuous PBDT-rich phase (pink regions) and a liquid-like phase (turquoise green regions). The densely connected high-aspect ratio of PBDT rods with homogeneously distributed liquid-like phases is presented in MIC.

parameters[10]. Multiphase PE systems can potentially achieve fast ion conduction via the mobile phase (for example, ionic liquids (ILs)) and desired mechanical properties by another rigid phase (for example, cross-linked polymer chains)[11,12]. However, the understanding of the interplay between chemistry and mechanics that drives any local phase transitions of PEs near the electrode|electrolyte interface is limited[13–17]. Unravelling the origin of interfacial chemomechanics and identifying the impact on the phase evolution of PEs could help develop the next generation of SSBs[18–22].

Investigating the concentration heterogeneity at the electrode|PE interface, that is, concentration polarization, could help understand intricate dynamics in SSBs affecting Li-ion flux and phase transitions of PEs. The local concentration heterogeneity can modulate the transport and mechanical properties of PEs, which can substantially impact the overall performance and stability of SSBs[16,23–25]. The local concentration polarization induces inhomogeneous current densities at the electrode|electrolyte interfaces, giving rise to localized hot spots for forming dendritic and dead lithium at the Li metal electrode|PE interface[26–28]. Another critical factor determining important aspects at SSB interfaces is chemical heterogeneity, which influences the evolution of interphases formed by interfacial side reactions. Hence, it is of utmost importance to track the evolution of concentration and chemical heterogeneities in PEs and directly visualize and analyse such heterogeneities in electrode|electrolyte interfaces of SSBs. Despite the importance of investigating concentration and chemical heterogeneities at the interfaces, there are a limited number of analytical techniques to probe the buried interfaces (that is, physically merged solid|solid interfaces between PE and electrodes) with chemical and spatial specificity in practical Li metal cell configuration[16,28–36].

Molecular ionic composite (MIC) electrolytes, which we use as a model electrolyte system (Fig. 1b), are a class of PEs showing robust mechanical properties (for example, stiffness >1 GPa modulus), high ionic conductivity (ranges from 1 mS cm^{-1} to 6 mS cm^{-1} at 30 °C) and wide electrochemical stability window (for example, 5.6 V versus $Li|Li^+$ at 25 °C)[37–42]. The high modulus (tensile moduli in the GPa range and shear moduli in the MPa range) of MICs stems from the self-assembly of charged rigid-rod (and double helical) ionic polymer (poly-2,2′-disulfonyl-4,4′-benzidine terephthalamide (PBDT)) with

smaller cations and anions (coming from a fluorinated Li salt or an imide-based IL) to form an electrostatic network[43,44]. These associative interactions form a two-phase system in MIC electrolyte at specific weight percentages of PBDT polymer: PBDT-rich phase and IL-rich liquid phase (Fig. 1b). Moreover, improved safety features of MIC are endowed by the low-flammability characteristics of the IL, Li salt and aromatic polyamide PBDT[45,46]. Indeed, MICs are already reported in the literature as tailorable building block materials for the preparation of solid-state electrolytes[37,47].

Herein, via X-ray fluorescence (XRF) microscopy and X-ray absorption spectroscopy (XAS) with high spatial resolution measurements and analyses, we elucidate concentration and chemical heterogeneities, their evolution across the electrode|electrolyte interfaces, and how they underpin and drive interfacial phase separation of PEs in high-potential Li metal cell configuration (Extended Data Fig. 1). We demonstrate that the conventional 'deformability' of PEs may not be sufficient to maintain intimate contact in electrode|PE interfaces in SSBs, especially when PEs undergo phase separation during electrochemical cycling. Furthermore, based on the knowledge acquired, we develop an interphase tailoring strategy using functional additives to passivate interfaces, aiming to suppress concentration and chemical heterogeneities to improve the battery performance.

Electrochemical characterizations of MIC electrolytes in Li metal cells

MICs represent a class of electrolyte materials comprising electrostatic interactions between the charged rigid-rod PBDT polymer and small mobile ions from ILs and lithium salts. These collective associative interactions give rise to an ionic conductive nanofibrillar 'bundle' phase, which enables the production of MICs with a single phase of 20–25 wt% PBDT. If the PBDT content is <20 wt%, MICs are a two-phase system, with the above-mentioned bundle phase co-continuous with an IL/salt-rich liquid phase that has a characteristic length scale <100 nm (refs. 39,41). The mechanical properties and ionic conductivities of MICs can be tuned by incorporating a wide selection of ILs and lithium salts. For battery electrolyte applications, MICs with a PBDT content of 10 wt% provide an ideal material platform for investigating interfacial degradation behaviour in multiphase PE systems.

The basic MIC electrolyte membrane in this study is composed of 10 wt% PBDT polymer with 10 wt% lithium bis(trifluoromethylsulfonyl) imide (LiTFSI) salt and 80 wt% 1-butyl-1-methylpyrrolidinium bis(trifluoromethylsulfonyl)imide (Pyr_{14}TFSI) IL. Supplementary Figs. 1–3 and Supplementary Note 1 provide the essential electrochemical characterization of the basic MIC electrolyte membrane. On the basis of the compositional tunability of MICs, 4.8 wt% lithium difluoro(oxalate)borate (LiDFOB) of lithium salt is incorporated into the basic MIC electrolyte as a functional additive for better cycling performance and termed as 'MIC with additive'. This material has the following composition: PBDT/LiTFSI/Pyr_{14}TFSI/LiDFOB in wt% of 9.5:9.5:76.2:4.8. Supplementary Fig. 4 shows photographic pictures and scanning electron microscopy (SEM) micrographs of the various MIC electrolyte samples before and after electrochemical measurements.

The Li||Li symmetric cells are cycled at 23 °C and 60 °C as a function of (stepped) current density to evaluate the compatibility between MIC membranes and Li metal electrodes (Fig. 2a). The potential response of Li||Li symmetric cells at 23 °C indicates the limiting current density with the basic MIC electrolyte to be 0.15 mA cm^{-2} and with the MIC with additive to be 0.25 mA cm^{-2}. At 23 °C, the MIC with additive showed lower overpotential throughout Li stripping and plating than the basic MIC (96 mV versus 403 mV, respectively, at 0.15 mA cm^{-2}). The lower overpotential and higher limiting current density of the MIC with additive at 23 °C suggest that a more stable interphase forms. At 60 °C, the limiting current density of the basic MIC is 0.65 mA cm^{-2}, and the MIC with additive is 0.5 mA cm^{-2}. The moderate limiting current density of MIC with additive compared with basic MIC may stem from the thickened passivation layer formed at 60 °C, which contributes to resistance and impedes efficient lithium plating and stripping. Li||Li symmetric cells tested with both types of MIC membrane at constant current density showed long-term cycling stability at 60 °C, lasting over 500 h (Supplementary Fig. 5).

On the basis of the ionic conductivity, mechanical strength and thermal stability of MIC electrolytes[38,42], Li|MIC|$LiNi_{0.8}Co_{0.1}Mn_{0.1}O_2$ (NMC811) coin cells were assembled to evaluate electrochemical energy storage performance. Figure 2b compares Li||NMC811 cells with basic MIC and MIC with additive electrolytes applying a cut-off potential of 4.4 V at 60 °C for 200 cycles at 67 mA g^{-1} (after two pre-conditioning cycles at 10 mA g^{-1}; Supplementary Fig. 6). The discharge capacity retention values after 200 cycles for Li||NMC811 cells with MIC with additive and basic MIC are 70% and 40%, respectively, demonstrating a beneficial effect of the LiDFOB additive in stabilizing battery performance[48]. Figure 2c shows the potential profiles during galvanostatic charge–discharge of the Li|MIC|NMC811 cell with a cut-off potential of 4.4 V at 60 °C, which delivers an initial specific discharge capacity of 217 mAh g^{-1} at 67 mA g^{-1} (after two pre-conditioning cycles at 10 mA g^{-1}; Supplementary Fig. 6) and specific discharge capacity retention of 60% after 100 cycles. Figure 2d shows the variation of the Li|MIC|NMC811 cell potential profiles with increasing specific current from 10 mA g^{-1} to 200 mA g^{-1}. The Li|MIC|NMC811 cell exhibited a maximum specific discharge capacity of 220 mAh g^{-1} at 10 mA g^{-1} and 110 mAh g^{-1} at 200 mA g^{-1}. Figure 2e shows the potential profiles during galvanostatic charge–discharge curves of the Li||NMC811 cell with MIC with additive applied with a cut-off potential of 4.4 V at 60 °C, delivering a maximum specific discharge capacity of 203 mAh g^{-1} at 67 mA g^{-1} (after two pre-conditioning cycles at 10 mA g^{-1}; Supplementary Fig. 6), and a specific discharge capacity retention of 83% after 100 cycles. The lower initial discharge capacity delivered by the cell with the MIC with additive compared with the basic MIC-based cell could be ascribed to the LiDFOB decomposition, which directly affects the impedance of the cell, as reported in the literature[48,49]. Figure 2f shows the variation of the potential profiles of the Li||NMC811 cell with MIC with additive, demonstrating a specific discharge capacity of about 185 mAh g^{-1} at 100 mA g^{-1}, which is about 17% higher than the Li|MIC|NMC811 cell at the same specific current.

Unlike in Li||Li symmetric cells, the MIC with additive electrolyte enables better performance in asymmetric Li||NMC811 cells because it forms a passivation layer (derived from the LiDFOB decomposition) that stabilizes the positive electrode|PE interface[48,50]. On the basis of these electrochemical characterizations, we carried out synchrotron X-ray measurements on Li||NMC811 with basic MIC and MIC with additive to understand the chemomechanical phenomena at the electrode|PE interfaces.

Investigating concentration heterogeneities at the electrode|MIC electrolyte interface

The XRF microscopy measurements enabled sulfur elemental mapping on cross-sections of the MIC electrolytes, unveiling the distribution of sulfur species therein[51,52]. The sulfonate group ($-SO_3^-$) of the rigid-rod polymer and the sulfone group ($-SO_2$) of the $TFSI^-$ anion from the IL and lithium salt contribute to the sulfur fluorescence signal. Considering the substantial portion of mobile ions (from both IL and lithium salt) in the MIC electrolytes (90 wt%), the sulfur fluorescence signal is dominated by the $TFSI^-$ anion. Hence, the mobile ion concentration in the MIC electrolytes can be directly visualized by XRF mapping, which can also reflect Li^+ concentration inferred from the charge-balancing counterion ($TFSI^-$).

Figure 3a–d shows sulfur XRF images of cross-sectioned samples examined ex situ and obtained for basic MIC electrolytes tested in Li||NMC811 cells applying various electrochemical testing conditions (Supplementary Figs. 7 and 8). The sulfur fluorescence counts per pixel (*X*-axis) versus the number of pixels (*Y*-axis) are plotted to compare each sample's ionic concentration distribution, which signals the degree of concentration heterogeneity. Moreover, the histogram

https://doi.org/10.1038/s41565-025-01885-5

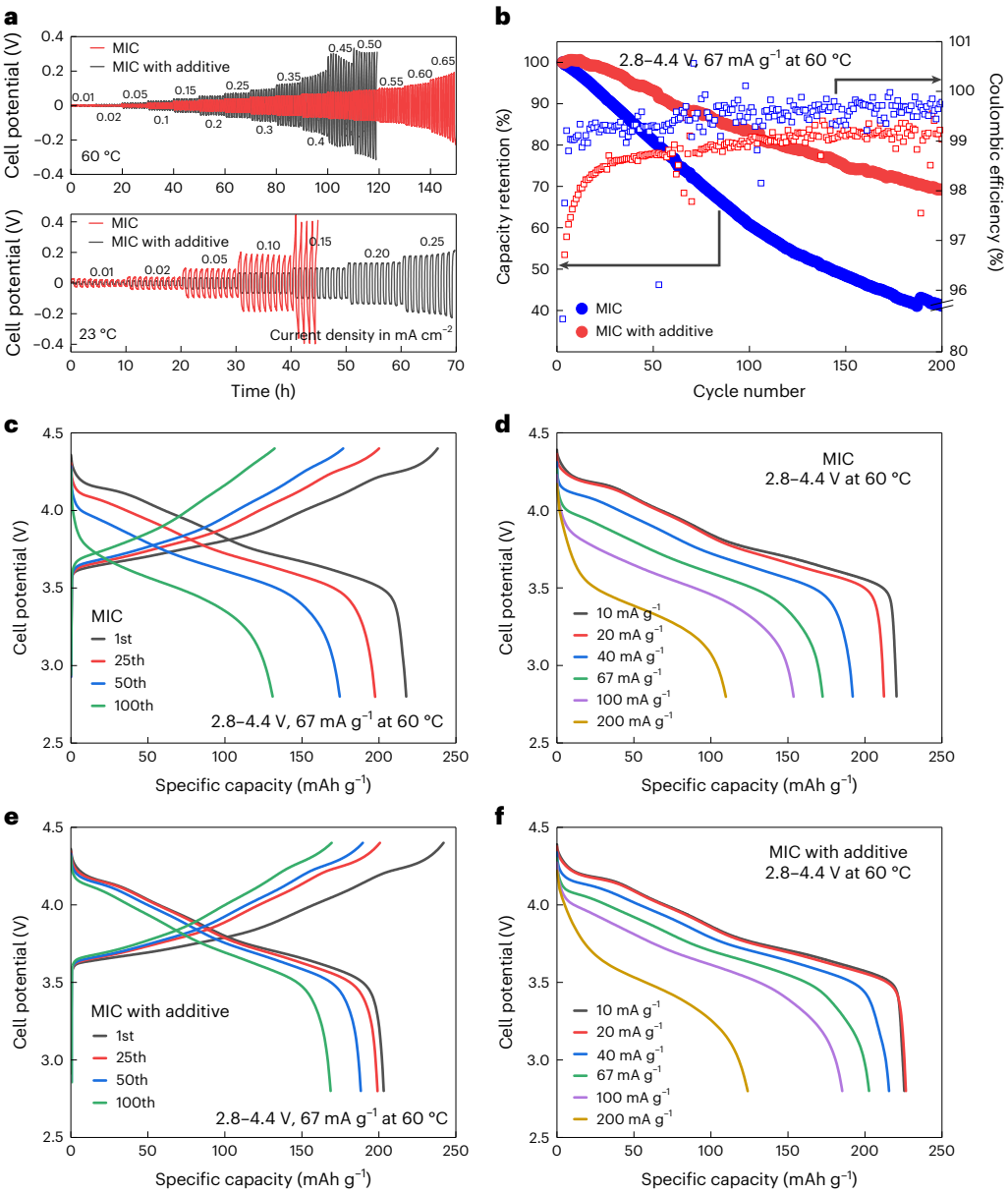

Fig. 2 | Electrochemical characterizations in symmetric and asymmetric cell configurations. a, Potential profiles of Li||Li symmetric cells cycled at 23 °C and 60 °C with increasing steps of current density. The charge and discharge time is 0.5 h, respectively, with current density increased every 10 cycles. **b**, Long-term cycling stability of Li|MIC|NMC811 and Li|MIC with additive|NMC811 cells at 2.8–4.4 V, 67 mA g^{-1} and 60 °C. **c**, Potential profiles of the Li|MIC|NMC811 cell at the 1st, 25th, 50th and 100th cycles at 2.8–4.4 V, 67 mA g^{-1} and 60 °C. **d**, Discharge potential profiles of the Li|MIC|NMC811 cell cycled at various specific currents at 60 °C in the cell potential range of 2.8–4.4 V. **e**, Potential profiles of the Li|MIC with the additive|NMC811 cell at the 1st, 25th, 50th and 100th cycles at 2.8–4.4 V, 67 mA g^{-1} and 60 °C. **f**, Discharge potential profiles of the Li|MIC with the additive|NMC811 cell cycled at various specific currents at 60 °C in the cell potential range of 2.8–4.4 V. The performance shown in **b**–**f** are obtained from Li||NMC811 cells with positive electrodes composed of 92 wt% active material, 4 wt% binder and 4 wt% conductive carbon. The performance of Li||NMC811 cells shown in **b**, **c** and **e** have been obtained after two pre-conditioning cycles at 10 mA g^{-1}. The initial two pre-conditioning cycles are shown in Supplementary Fig. 6.

area corresponds to the total intensity of the sulfur fluorescence signal obtained from the XRF image. The pristine basic MIC electrolyte shows a uniform distribution of mobile ions with a narrow range of sulfur fluorescence counts per pixel (Fig. 3a). The cross-sectional XRF image of the basic MIC electrolyte membrane collected from the assembled coin cell rested at 60 °C and open-circuit potential (OCP) for 1 day is shown in Fig. 3b. Comparing Fig. 3a and Fig. 3b, it is noticeable that the pressure applied during cell assembly (0.2 MPa) alone does not cause substantial depletion of mobile ion concentration at the electrode|PE interface. In Fig. 3c, after 8 charge/discharge cycles (2.8–4.4 V, 67 mA g^{-1} and 60 °C) in the Li||NMC811 cell, the collected basic MIC electrolyte membrane shows a wide distribution of sulfur fluorescence intensity compared with pristine basic MIC and basic MIC rested samples. This change in the distribution of sulfur fluorescence intensity of the basic MIC membrane may indicate the onset of concentration heterogeneity depending on electrochemical cycling protocols.

After 200 charge/discharge cycles (2.8–4.4 V, 67 mA g^{-1} and 60 °C) in the Li||NMC811 cell (Fig. 3d), the concentration heterogeneity of the MIC membrane increases substantially, which resonates with the broadened distribution of sulfur fluorescence counts per pixel. The observed concentration heterogeneity may likely result from a disruption in MIC's two-phase system, which begins from the decomposition of rigid-rod ionic PBDT polymer at the electrode|PE interface (Supplementary Figs. 9 and 10 and Supplementary Notes 2 and 3).

https://doi.org/10.1038/s41565-025-01885-5

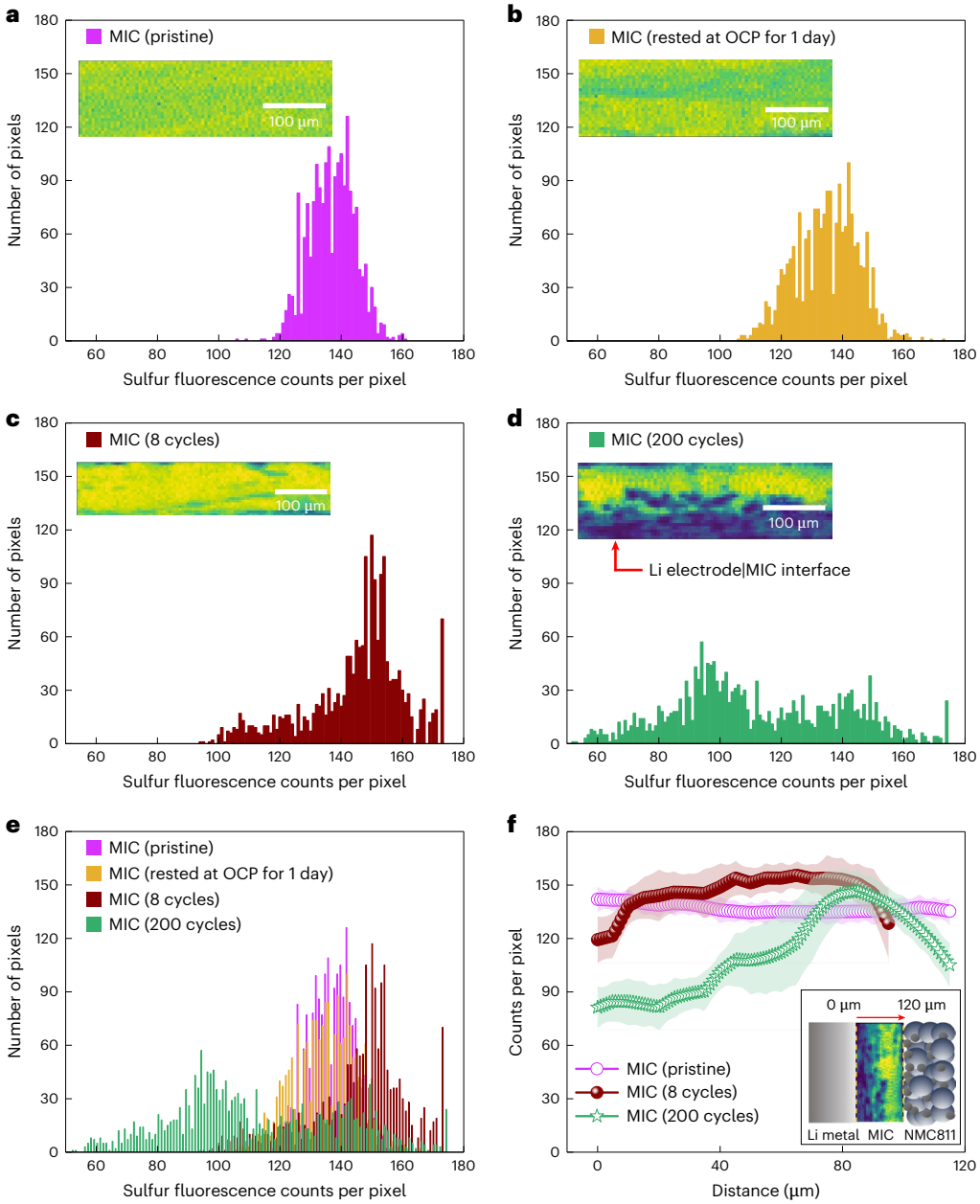

Fig. 3 | Map and visualization of sulfur-containing ion distribution in basic MIC PEs via ex situ XRF measurements. The tender energy X-ray synchrotron enables the imaging of sulfur species distribution of MIC electrolyte, indicating local ionic concentration heterogeneity in the context of Li||NMC811 cell configuration. The XRF images are obtained by scanning an X-ray beam size of 5 µm with a 15 µm probing depth. The representative area of the XRF image from each sample is chosen for comparison and shown in the insets. The histogram of the sulfur fluorescence signal is shown in **a**–**e** as sulfur fluorescence counts per pixel (*X*-axis) versus number of pixels (*Y*-axis). White scale bars are all 100 µm. The sulfur fluorescence counts per pixel represent the relative population of sulfur species within the probed region of the X-ray beam, where bright yellow pixels indicate a higher population of sulfur species while dimmer green pixels present a lower population (inset of **a**–**d**). **a**–**d**, Pristine MIC (before cell assembly) (**a**), MIC (rested at OCP after cell assembly for 1 day) (**b**), MIC (8 cycles at 67 mA g^{-1} and 60 °C in the potential cell range of 2.8–4.4 V) (**c**) and MIC (200 cycles at 67 mA g^{-1} and 60 °C in the potential cell range of 2.8–4.4 V) (**d**). **e**, Overlay of **a**–**d**. The plot of the sulfur fluorescence signal across the Li metal negative electrode|electrolyte interface to the electrolyte|positive electrode interface is shown in **f** as distance (*X*-axis) versus sulfur fluorescence counts per pixel (*Y*-axis). The averaged sulfur fluorescence intensity is plotted in points, and the standard deviations are in shades (**f**). **f**, Pristine MIC, MIC (8 cycles) and MIC (200 cycles).

The discrepancy between the XRF image of the pristine MIC and MIC (200 cycles) sample suggests that a cumulative concentration heterogeneity occurred throughout the extensive electrochemical cycling (Fig. 3d). Considering that the area of the histogram between MIC (pristine) and MIC (200 cycles) is unchanged, it is likely that the sulfur species are heterogeneously redistributed rather than extracted outward from the MIC membrane (Supplementary Fig. 11 and Supplementary Note 4). Furthermore, the SEM images of the cross-sectional cycled MIC membranes tested in Li||Li and Li||NMC811 cells show a clear edge with preserved thickness (Supplementary Figs. 12 and 13 and Supplementary Note 5). The synchrotron micro-computed tomography measurements suggest the lack of discernable pores inside pristine or cycled MIC membranes, thus supporting the speculation that concentration heterogeneity observed in XRF images does not originate from void, dead lithium or lithium dendrite (Supplementary Fig. 14 and Supplementary Note 6). Localized regions depleted of sulfur fluorescence

signal are particularly evident at the interfaces, especially at the Li metal|MIC electrolyte interface (Fig. 3d). The overlay of the histogram from cross-sectional MIC samples indicates that sulfur fluorescence intensity becomes widely distributed after cell cycling, indicating the presence of concentration heterogeneities (Fig. 3e).

The local concentration heterogeneity at the electrode|MIC electrolyte interface imposes constraints in uniform Li^+ flux, ensuing nonuniform current density. As a consequence, this concentration nonuniformity at the interface induces localized 'hot spots', intensifying the degradation of the PE, promoting lithium dendrite growth and facilitating the formation of dead lithium at the Li negative electrode|MIC electrolyte interface, leading to rapid cell capacity decay[26,27]. In addition, the concentration heterogeneity brings about phase transition in MIC electrolytes by disrupting the 'PBDT-rich' and 'IL-rich' phases, thereby undermining the mechanical integrity of the PE membrane. Consequently, the erratic population of low-sulfur fluorescence domains prevailing at electrode|MIC electrolyte interfaces indicates chemical and mechanical degradations of the MIC PE (Supplementary Fig. 8).

The line profile analysis provides further insights into changes in ion concentration as a function of distance from a specific interface, as shown in Fig. 3f with distance from the negative electrode|electrolyte interface (*X*-axis) versus sulfur fluorescence counts per pixel (*Y*-axis). The uniform ion concentration distribution in pristine MIC is shown as a plateau in counts per pixel, irrespective of location (Fig. 3f). In the sulfur fluorescence intensity line profile of MIC (after 8 cycles in Li||NMC811 cell), a decrease in the sulfur fluorescence counts per pixel is observed at the negative electrode|electrolyte interface ($X = 0–10$ μm) and positive electrode|electrolyte interface ($X = 90–100$ μm), presumably owing to the breakdown of the two-phase structure of the MIC possibly originated by side reactions with the electrodes (Supplementary Fig. 9 and Supplementary Note 2). The MIC (after 200 cycles in Li||NMC811 cell) sample showed drastic changes in sulfur fluorescence counts per pixel along the direction between two interfaces (Fig. 3f). This inhomogeneous sulfur fluorescence intensity across the MIC (200 cycles) suggests that concentration heterogeneity initiated at the electrode|MIC electrolyte interfaces eventually propagates towards the bulk of the MIC electrolyte membrane. Figure 3f shows a notable decrease in the sulfur fluorescence counts per pixel at the negative electrode|electrolyte interface spanning the bulk region ($X = 0–90$ μm). The prominent concentration heterogeneity at the Li negative electrode|electrolyte interface suggests the breakdown of the two phases in the MIC electrolyte. Concentration heterogeneity is shown throughout the 30 μm region ($X = 90–120$ μm) for the positive electrode|electrolyte interface. Considering the degree of concentration heterogeneity observed in line profile analysis, the Li negative electrode|electrolyte interface is more pronounced with phase separation. The observed concentration heterogeneity may likely result from a disruption in MIC's two-phase system, which begins from the decomposition of rigid-rod ionic PBDT polymer at the Li metal negative electrode interface[35,53] (Supplementary Fig. 10). Moreover, the degree of concentration heterogeneity is relevant to the upper cut-off potential of the cycling condition, which aligns with our proposed decomposition pathways (Supplementary Figs. 10 and 15–18, and Supplementary Note 7). The high cut-off potential applied during cell cycling accelerates the decomposition of charged rigid-rod PBDT polymer into short oligomers and by-products that no longer maintain the uniform distribution of the liquid-like phase in the two-phase electrolyte system.

The role of the chemical heterogeneities on the evolution of the interphase formed at the electrode|MIC electrolyte interfaces

Sulfur K-edge XAS measurements directly probe the chemical nature of sulfur within the cross-sectional sample of the MIC electrolyte by studying the characteristic transitions corresponding to different sulfur species. Combined with the XRF mapping, the point scanning XAS on cross-sectional samples allowed site-specific probing of sulfur chemical states, particularly across electrode|electrolyte interfaces. On the basis of the XRF image from the cross-section of the Li||NMC811 cell, the analyses of the ex situ XAS measurements suggest the presence of sulfur species at the electrode|electrolyte interfaces, which are not detectable via X-ray photoelectron spectroscopy (XPS) measurements (Supplementary Figs. 19–21 and Supplementary Note 8).

The XAS investigation on the MIC electrolytes (basic and with additive) and their components aligned with previous reports of sulfur X-ray absorption near edge structure (XANES) results[54–58] (Supplementary Fig. 22). The basic MIC electrolyte features a broad maximum at 2,480.5 eV, a composite of sulfone and sulfonate groups (Supplementary Fig. 22e).

We also carried out ex situ XAS measurements and analyses on the MIC electrolyte sampled after 8 cycles (at 67 mA g^{-1} and 60 °C in the potential cell range of 2.8–4.4 V in Li||NMC811 cell configuration; Fig. 4a). From point A, the lowest-energy feature at 2,473.9 eV is assigned as the $S_{1s} \rightarrow \sigma^*$(S-C) transition, which identifies the presence of low-valent sulfur species[54,58,59] (Fig. 4a). This energy feature supports the claim of the reductive decomposition of the MIC electrolyte at the interface with the Li metal negative electrode, attributed to sulfide species, as suggested in the reaction pathway disclosed in Supplementary Figs. 23 and 24, and Supplementary Note 9. Other types of sulfur species are not observed in points B and C, possibly owing to the early stage of cell cycling (that is, only 8 cycles carried out before the ex situ spectroscopy measurements).

For the MIC (200 cycles) sample, ex situ synchrotron measurements are carried out only for the MIC membrane without taking into account the Li and NMC811 electrodes (Fig. 4b). From region C in MIC (200 cycles), a feature at 2,482.0 eV is observed and attributed to high-valent sulfur species, that is, S^{6+} as SO_4^{2-} (sulfate)[55]. This feature may have originated from the oxidative decomposition of MIC electrolyte at the interface with the positive electrode (region C) as the chemical pathway suggested in Supplementary Figs. 23 and 24 and Supplementary Note 9, which is shifted to higher energy by ~1.4 eV than pristine MIC (Fig. 4b).

In addition, the feature at 2,473.6 eV, at region C of the positive electrode|electrolyte interface, corresponds to the transition metal chelated to the sulfonate group of MIC electrolyte, that is, $S_{1s} \rightarrow \sigma^*(M_{3d}\text{-}S)$[57]. However, despite the long cycling, the reductively decomposed sulfur species are not observed in the sample. Initially, we assumed that the XANES feature corresponding to reductive decomposition might have been lost during the collecting, sampling and transporting procedures of the MIC membrane for the ex situ measurement. However, XANES spectra corresponding to reductive decomposition are observed in other MIC samples (Supplementary Fig. 18), indicating that cross-sectional membrane samples are sufficient to probe interphase evolution as long as enough point scans are conducted.

Along with the concentration heterogeneity, chemical heterogeneity accounts for the degradation of PEs at the electrode|electrolyte interface, undermining the structural integrity and transport properties of the PE membrane (Fig. 5 and Supplementary Figs. 23 and 24). The spatially resolved XAS measurements and analyses on the corresponding sulfur fluorescence image inform the evolution of interphase in a statistically wide field of view on the cross-sectional Li||NMC811, providing additional insights into interfacial chemical speciation. The concentration and chemical heterogeneity are also observed in other types of PE, suggesting that interfacial heterogeneity is a widespread phenomenon (Supplementary Figs. 25–33 and Supplementary Note 10), which should be taken into account for developing electrochemically stable PEs for battery applications.

Morphological evolutions and ion transport mechanisms behaviour in MIC electrolytes

We investigated MIC electrolytes' surface morphology and ion diffusion properties to understand interfacial phase separation. The characteristic internal microstructure of MIC and its evolution after

https://doi.org/10.1038/s41565-025-01885-5

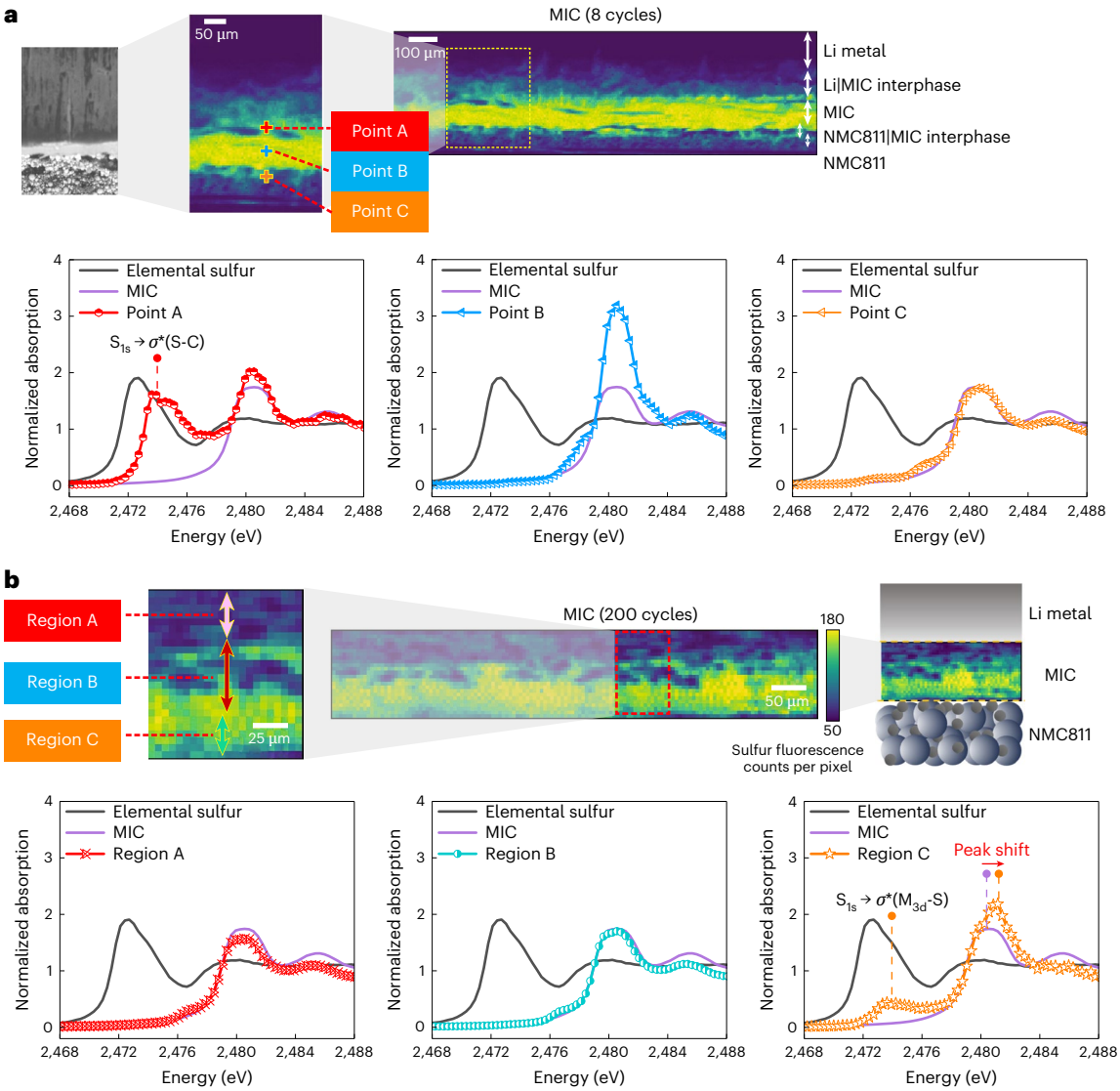

Fig. 4 | Spatially resolved chemical analyses in basic MIC PE. The site-specific S K-edge XAS ex situ measurements show the evolution of interphase associated with the presence of chemical heterogeneity. The XRF S mapping image and corresponding site-specific XANES spectra with the characteristic transitions of S are shown (the reductive decomposition is revealed in point A from panel **a**, while oxidative decomposition is revealed in region C of panel **b**). XANES figures from both **a** and **b** contain elemental sulfur (S_8) (grey) and pristine MIC (light purple) as reference spectra. The sample preparation for synchrotron measurements is described in Methods. Supplementary Fig. 22 provides XANES spectra of reference samples. XANES feature of point or region is obtained by an X-ray beam size of 5 µm with a 15 µm probing depth. **a**, MIC (8 cycles at 67 mA g^{-1} and 60 °C in the potential cell range of 2.8–4.4 V, entire cell cross-section). **b**, MIC (200 cycles at 67 mA g^{-1} and 60 °C in the potential cell range of 2.8–4.4 V, cell disassembled and only electrolyte membrane was measured).

electrochemical cycling (in Li||NMC811 cell configuration) with respect to specific electrode|electrolyte interfaces is studied by atomic force microscopy (AFM). Figure 5a–c shows the topographic image of the pristine, positive electrode-facing and negative electrode-facing sides of the MIC membrane, where bright and dark areas correspond to higher and lower heights, respectively. In Fig. 5a, the extensive bright areas of the pristine MIC (before cell assembly) AFM image correspond to the nanofibrillar 'bundle' phase in the width of 20–40 nm of interconnected fibrillar network with low surface roughness (R_q = 3.01 nm, root-mean-square roughness). The dark area in the AFM image of pristine MIC corresponds to the IL-rich liquid phase (Fig. 5a). In Fig. 5b, the electrochemically cycled positive electrode-facing MIC surface exhibits raised (bright area) and sunken regions (dark area) with high surface roughness (R_q = 8.81 nm) and the segregation of bundle phase in the width of 80–100 nm. In Fig. 5c, the negative electrode-facing side of the MIC showed surface roughness (R_q = 13.6 nm) and deformation, as indicated by large sunken regions, which are ascribed to volumetric change during lithium stripping and plating at the interface. In addition, dead lithium particles are observed at the surface of the negative electrode-facing MIC. These electrodepositions are associated with the nonuniform ionic flux at the interface owing to concentration heterogeneity (Fig. 5c). Figure 5d shows the height profile of three samples with 2 µm length, revealing the increase of surface roughness after electrochemical cycling. The electrochemically induced phase evolution of the MIC electrolyte results in the loss of ionically conductive phase at the interface and decline of surface modulus up to a factor of 2 (Fig. 5e). The AFM study provides insights into the electrochemically induced phase evolution of MIC, which supports the concentration heterogeneity observed in XRF maps, thereby leading to the detachment of the ionically conductive phase of the PE membrane at the interface with the cell electrode (Supplementary Fig. 9 and Supplementary Note 2).

The ion transport behaviour of MIC electrolyte is investigated by ex situ pulsed-field-gradient nuclear magnetic resonance (NMR) diffusometry measurements in the 25–80 °C temperature range, by

https://doi.org/10.1038/s41565-025-01885-5

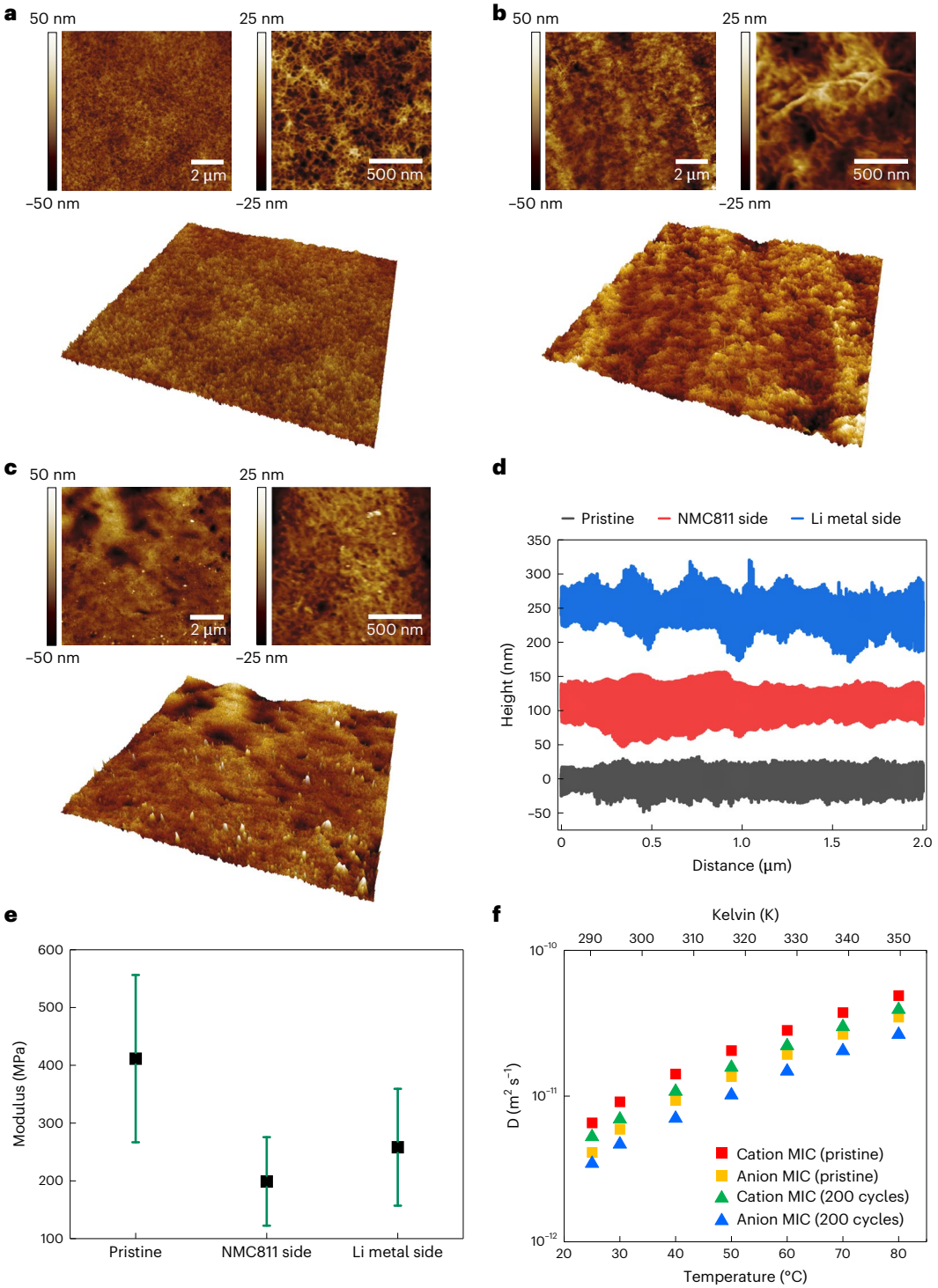

Fig. 5 | The evolution of surface morphology and diffusion properties of electrochemically cycled MIC electrolyte. Topographic scanning unveils morphological changes in the MIC membrane surface. The pulsed-field-gradient NMR diffusometry measurements reveal the changes in the ion transport behaviour of MIC electrolytes after electrochemical cycling. The cycled MIC electrolyte shown here is after 200 cycles at 67 mA g^{-1} and 60 °C in the potential cell range of 2.8–4.4 V. **a**–**c**, AFM image in height maps and three-dimensional representation of corresponding height maps of pristine MIC (before cell assembly) (**a**), electrochemically cycled positive electrode-facing MIC (**b**) and negative electrode-facing MIC (**c**). **d**, Surface roughness profile of each AFM image. **e**, Modulus plot of MIC membranes (the error bars indicate the standard deviation obtained from 100 scanned regions). **f**, Temperature-dependent diffusion coefficient plots of pristine MIC and MIC electrolyte after 200 cycles at 67 mA g^{-1} in the potential cell range of 2.8–4.4 V.

measuring the self-diffusion coefficients for the IL cations (^{1}H NMR) and IL anions (^{19}F NMR)[37]. Figure 5f shows cation diffusion coefficients (D^+) and the anion diffusion coefficients (D^-) of pristine and cycled MIC (200 cycles at 67 mA g^{-1} in the potential cell range of 2.8–4.4 V) at various temperatures and averaged over the entire electrolyte thickness. In both the pristine MIC and cycled MIC, a faster diffusion of cations than anions is observed throughout the temperature range. The cycled MIC shows 22% decreased D^+ and D^- compared with pristine MICs, suggesting that ion transport properties averaged over the whole MIC sample have changed after electrochemical cycling. The total ionic diffusion

https://doi.org/10.1038/s41565-025-01885-5

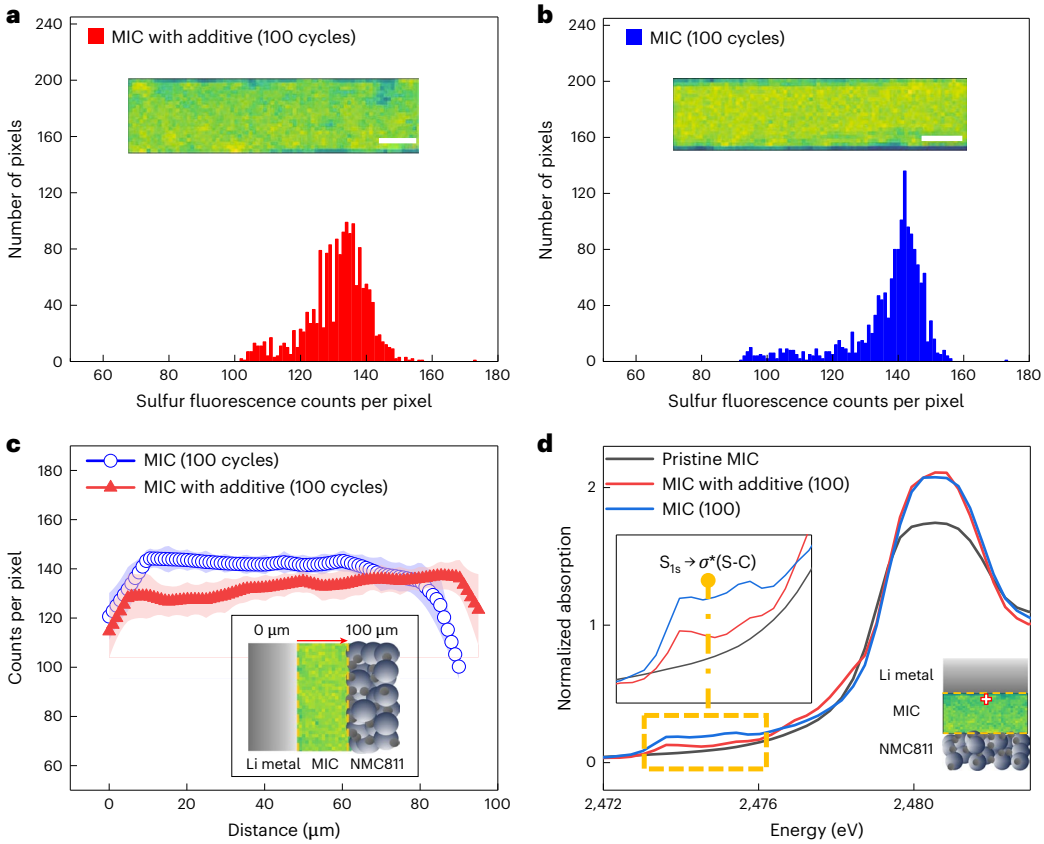

Fig. 6 | Evaluating the impact of additives on concentration and chemical heterogeneities in MIC electrolytes via XRF and XAS measurements. Tender energy X-ray synchrotron measurements and analyses enable structure and chemical interrogation of the role of the additive in the degradation of MIC electrolytes. The XRF images (inset pictures of **a** and **b**) are obtained by scanning an X-ray beam size of 5 µm with a 15 µm probing depth. The representative area of the XRF image from each sample is chosen for comparison. The histogram of sulfur fluorescence signal is shown in **a** and **b** as sulfur fluorescence counts per pixel (*X*-axis) versus number of pixels (*Y*-axis). White scale bars are all 50 µm. The sulfur fluorescence counts per pixel represent the relative population of sulfur species within the probed region of the X-ray beam, where bright yellow pixels indicate a higher population of sulfur species while dimmer green pixels present a lower population. **a**,**b**, MIC with additive (**a**) and MIC (**b**) (both tested in Li||NMC811 cell configuration at 67 mA g^{-1} and 60 °C in the potential cell range of 2.8–4.4 V). **c**, The plot of the sulfur fluorescence signal across the negative electrode|electrolyte interface to the electrolyte|positive electrode interface: MIC (100 cycles) and MIC with additive (100 cycles) (both in full cells). The averaged sulfur fluorescence intensity is plotted in points, and the standard deviations are in shades. **d**, The set of XRF images, XANES spectra collected at point A (cross mark) and scheme of cell components: MIC (100 cycles) and MIC with additive (100 cycles). The box with the yellow outline shows the energy range for the product from the reductive decomposition of sulfone and sulfonate species.

coefficients (*D*, the summation of the cation and anion diffusion coefficients) of pristine MIC and cycled MIC are $4.8 \pm 0.2 \times 10^{-11}$ m^2 s^{-1} and $3.7 \pm 0.2 \times 10^{-11}$ m^2 s^{-1}, respectively, at 60 °C, which is a 23% decrease owing to electrochemical cycling effect. From the XRF imaging, we can infer that the decrease in ionic diffusivities is more pronounced near the electrode interfaces than the 23% decrease obtained from these measurements. These diffusion coefficient results indicate that interfacial concentration and chemical heterogeneity affect bulk ion transport properties, eventually contributing to cell failure. The worsened transport properties originate from the regions close to the interfaces. When the electrolyte becomes very thin (<20 µm), and the interfacial region represents a large fraction of the electrolyte, the interfacial heterogeneity may completely shut down the ion transport between the positive and negative electrodes in the cell.

The role of additives in mitigating concentration and chemical heterogeneities in MIC electrolytes

On the basis of our demonstration that the concentration and chemical heterogeneities drive the degradation of MIC electrolytes, the role of additives is investigated using synchrotron X-ray measurements. MIC and MIC with additive samples, collected after 100 cycles at 67 mA g^{-1} and 60 °C in the potential cell range of 2.8–4.4 V, are investigated to evaluate the extent of concentration and chemical heterogeneities. To evaluate the influence of additives on ionic concentration profile, we considered comparable sizes of the cross-sectional sample, that is, MIC (400 × 95 $µm^2$) and MIC with additive (400 × 100 $µm^2$). The MIC presented a higher of concentration heterogeneity compared with the MIC with additive (Fig. 6a,b), showing an elongated tail in the histogram. In Fig. 6c, the line profile analysis shows the sulfur fluorescence signal with respect to distance from interfaces of MIC and MIC with additive. The MIC and MIC with additive show relatively homogeneous ion concentration distribution within the bulk region (20–80 µm). However, MIC shows an abrupt decline of sulfur counts per pixel at interfaces: a 16.4% decrease at the negative electrode|electrolyte interface (0–10 µm) and a 25.9% decrease at the positive electrode|electrolyte interface (78–90 µm). On the other hand, MIC with additive shows a lower degree of sulfur fluorescence signal decline at interfaces: an 11% decrease at the negative electrode|electrolyte interface (0–10 µm) and a 9.8% decrease at the positive electrode|electrolyte interface (78–90 µm). The lower degree of concentration depletion at the positive electrode|electrolyte interface aligns with the beneficial effect of LiDFOB on stabilizing the positive electrode|electrolyte interface. Therefore, considering the lower standard deviation from sulfur fluorescence counts per pixel histogram of MIC with additive (Fig. 6a,b) and its mitigated concentration

decline at interfaces (Fig. 6c), the additive has proven effective in ameliorating concentration heterogeneity.

Figure 6d shows XAS measurements and analyses to identify chemical species evolved from interfacial side reactions. The MIC with additive electrolyte shows suppressed chemical heterogeneity at the negative electrode|electrolyte interface compared with the basic MIC. This behaviour is possibly associated with the presence of the passivation layer formed by LiDFOB decomposition, which mitigates the reductive decomposition of the PE (Fig. 6d).

Conclusion

In summary, in this research work, we carried out fundamental investigations of the phase separation phenomenon within MIC electrolytes owing to interfacial degradation in Li||NMC811 cell configuration. This degradation leads to the deterioration of the ionically conductive phase at the electrode|electrolyte interface and the emergence of an ionic depletion region. Interfacial heterogeneity eventually leads to a decline in mechanical properties and ion diffusion properties of MIC electrolyte. We expect that such interfacial issues can be exacerbated when the PE is thin (<20 μm), and the interfacial region represents a considerable fraction of the electrolyte. Through our investigation, MIC has emerged as a valuable model to extend investigations of interfacial phase separation behaviour within multiphase PEs. The sulfur compounds present in MIC electrolytes act as an indicator, allowing us to track the evolution of ionic concentration and interphase development using the combined analyses of XRF microscopy and XAS measurements. Such a combination enables to carry out analyses with spatial precision, revealing the intricate structure and chemistry of buried interfaces within electrochemical cells with PEs on a statistically significant scale. The direct visualization of local concentration heterogeneity and site-specific chemical analysis of electrode|electrolyte interfaces provided fundamental insights into regulating interfacial chemomechanics using functional additives, which could help improving the research on PEs for battery applications.

Online content

Any methods, additional references, Nature Portfolio reporting summaries, source data, extended data, supplementary information, acknowledgements, peer review information; details of author contributions and competing interests; and statements of data and code availability are available at https://doi.org/10.1038/s41565-025-01885-5.

References

1. Manthiram, A., Yu, X. & Wang, S. Lithium battery chemistries enabled by solid-state electrolytes. *Nat. Rev. Mater.* **2**, 1–16 (2017).
2. Wan, J. et al. Ultrathin, flexible, solid polymer composite electrolyte enabled with aligned nanoporous host for lithium batteries. *Nat. Nanotechnol.* **14**, 705–711 (2019).
3. Choudhury, S. Solid-state polymer electrolytes for high-performance lithium metal batteries. *Nat. Commun.* **10**, 4398 (2019).
4. Christie, A. M., Lilley, S. J., Staunton, E., Andreev, Y. G. & Bruce, P. G. Increasing the conductivity of crystalline polymer electrolytes. *Nature* **433**, 50–53 (2005).
5. Dong, T. et al. A multifunctional polymer electrolyte enables ultra-long cycle-life in a high-voltage lithium metal battery. *Energy Environ. Sci.* **11**, 1197–1203 (2018).
6. Zhao, Q., Liu, X., Stalin, S., Khan, K. & Archer, L. A. Solid-state polymer electrolytes with in-built fast interfacial transport for secondary lithium batteries. *Nat. Energy* **4**, 365–373 (2019).
7. Hatzell, K. B. et al. Challenges in lithium metal anodes for solid-state batteries. *ACS Energy Lett.* **5**, 922–934 (2020).
8. Wang, X. et al. Toward high-energy-density lithium metal batteries: opportunities and challenges for solid organic electrolytes. *Adv. Mater.* **32**, 1905219 (2020).
9. Glynos, E., Pantazidis, C. & Sakellariou, G. Designing all-polymer nanostructured solid electrolytes: advances and prospects. *ACS Omega* **5**, 2531–2540 (2020).
10. Lu, G. et al. Trade-offs between ion-conducting and mechanical properties: the case of polyacrylate electrolytes. *Carbon Energy* **5**, e287 (2023).
11. Gu, Y. et al. High toughness, high conductivity ion gels by sequential triblock copolymer self-assembly and chemical cross-linking. *J. Am. Chem. Soc.* **135**, 9652–9655 (2013).
12. Cho, B. K., Jain, A., Gruner, S. M. & Wiesner, U. Mesophase structure-mechanical and ionic transport correlations in extended amphiphilic dendrons. *Science* **305**, 1598–1601 (2004).
13. Grundy, L. S. et al. Inaccessible polarization-induced phase transitions in a block copolymer electrolyte: an unconventional mechanism for the limiting current. *Macromolecules* **55**, 7637–7649 (2022).
14. Galluzzo, M. D., Loo, W. S., Schaible, E., Zhu, C. & Balsara, N. P. Dynamic structure and phase behavior of a block copolymer electrolyte under dc polarization. *ACS Appl. Mater. Interfaces* **12**, 57421–57430 (2020).
15. Virgili, J. M., Nedoma, A. J., Segalman, R. A. & Balsara, N. P. Ionic liquid distribution in ordered block copolymer solutions. *Macromolecules* **43**, 3750–3756 (2010).
16. Gomez, E. D. et al. Effect of ion distribution on conductivity of block copolymer electrolytes. *Nano Lett.* **9**, 1212–1216 (2009).
17. Choi, J. H., Ye, Y., Elabd, Y. A. & Winey, K. I. Network structure and strong microphase separation for high ion conductivity in polymerized ionic liquid block copolymers. *Macromolecules* **46**, 5290–5300 (2013).
18. Koerver, R. et al. Chemo-mechanical expansion of lithium electrode materials—on the route to mechanically optimized all-solid-state batteries. *Energy Environ. Sci.* **11**, 2142–2158 (2018).
19. Lewis, J. A. et al. Interphase morphology between a solid-state electrolyte and lithium controls cell failure. *ACS Energy Lett.* **4**, 591–599 (2019).
20. Lewis, J. A. et al. Linking void and interphase evolution to electrochemistry in solid-state batteries using operando X-ray tomography. *Nat. Mater.* **20**, 503–510 (2021).
21. Tippens, J. et al. Visualizing chemomechanical degradation of a solid-state battery electrolyte. *ACS Energy Lett.* **4**, 1475–1483 (2019).
22. Lewis, J. A., Tippens, J., Cortes, F. J. Q. & McDowell, M. T. Chemo-mechanical challenges in solid-state batteries. *Trends Chem.* **1**, 845–857 (2019).
23. Sharon, D. et al. Molecular level differences in ionic solvation and transport behavior in ethylene oxide-based homopolymer and block copolymer electrolytes. *J. Am. Chem. Soc.* **143**, 3180–3190 (2021).
24. Chintapalli, M. et al. Structure and ionic conductivity of polystyrene-block-poly(ethylene oxide) electrolytes in the high salt concentration limit. *Macromolecules* **49**, 1770–1780 (2016).
25. Shen, K. H. & Hall, L. M. Ion conductivity and correlations in model salt-doped polymers: effects of interaction strength and concentration. *Macromolecules* **53**, 3655–3668 (2020).
26. Lee, Y., Ma, B. & Bai, P. Overlimiting ion transport dynamic toward Sand's time in solid polymer electrolytes. *Mater. Today Energy* **27**, 101037 (2022).
27. Lee, Y., Ma, B. & Bai, P. Concentration polarization and metal dendrite initiation in isolated electrolyte microchannels. *Energy Environ. Sci.* **13**, 3504–3513 (2020).
28. Cheng, Q. et al. Operando and three-dimensional visualization of anion depletion and lithium growth by stimulated Raman scattering microscopy. *Nat. Commun.* **9**, 2942 (2018).
29. Devaux, D. et al. Failure mode of lithium metal batteries with a block copolymer electrolyte analyzed by X-ray microtomography. *J. Electrochem. Soc.* **162**, A1301–A1309 (2015).

30. Kaboli, S. et al. Behavior of solid electrolyte in Li-polymer battery with NMC cathode via in-situ scanning electron microscopy. *Nano Lett.* **20**, 1607–1613 (2020).
31. Harry, K. J., Hallinan, D. T., Parkinson, D. Y., MacDowell, A. A. & Balsara, N. P. Detection of subsurface structures underneath dendrites formed on cycled lithium metal electrodes. *Nat. Mater.* **13**, 69–73 (2013).
32. Golozar, M. et al. In situ scanning electron microscopy detection of carbide nature of dendrites in Li-polymer batteries. *Nano Lett.* **18**, 7583–7589 (2018).
33. Maslyn, J. A. et al. Growth of lithium dendrites and globules through a solid block copolymer electrolyte as a function of current density. *J. Phys. Chem. C* **122**, 26797–26804 (2018).
34. Harry, K. J., Liao, X., Parkinson, D. Y., Minor, A. M. & Balsara, N. P. Electrochemical deposition and stripping behavior of lithium metal across a rigid block copolymer electrolyte membrane. *J. Electrochem. Soc.* **162**, A2699–A2706 (2015).
35. Andersson, E. K. W. et al. Early-stage decomposition of solid polymer electrolytes in Li-metal batteries. *J. Mater. Chem. A* **9**, 22462–22471 (2021).
36. Zhang, X. et al. Multi-scale characterization techniques for polymer-based solid-state lithium batteries. *Macromol. Chem. Phys.* **224**, 2200351 (2023).
37. Bostwick, J. E. et al. Ionic interactions control the modulus and mechanical properties of molecular ionic composite electrolytes. *J. Mater. Chem. C* **10**, 947–957 (2022).
38. Yu, D. et al. Room temperature to 150 °C lithium metal batteries enabled by a rigid molecular ionic composite electrolyte. *Adv. Energy Mater.* **11**, 2003559 (2021).
39. Fox, R. J. et al. Nanofibrillar ionic polymer composites enable high-modulus ion-conducting membranes. *ACS Appl. Mater. Interfaces* **11**, 40551–40563 (2019).
40. Wang, Y. et al. Highly conductive and thermally stable ion gels with tunable anisotropy and modulus. *Adv. Mater.* **28**, 2571–2578 (2016).
41. Bostwick, J. E. et al. Ion transport and mechanical properties of non-crystallizable molecular ionic composite electrolytes. *Macromolecules* **53**, 1405–1414 (2020).
42. Wang, Y. et al. Solid-state rigid-rod polymer composite electrolytes with nanocrystalline lithium ion pathways. *Nat. Mater.* **20**, 1255–1263 (2021).
43. Wang, Y. Double helical conformation and extreme rigidity in a rodlike polyelectrolyte. *Nat. Commun.* **10**, 801 (2019).
44. Yu, Z., He, Y., Wang, Y., Madsen, L. A. & Qiao, R. Molecular structure and dynamics of ionic liquids in a rigid-rod polyanion-based ion gel. *Langmuir* **33**, 322–331 (2017).
45. Forsyth, M., Porcarelli, L., Wang, X., Goujon, N. & Mecerreyes, D. Innovative electrolytes based on ionic liquids and polymers for next-generation solid-state batteries. *Acc. Chem. Res.* **52**, 686–694 (2019).
46. Hasanpoor, M. et al. Morphological evolution and solid-electrolyte interphase formation on $LiNi_{0.6}Mn_{0.2}Co_{0.2}O_2$ cathodes using highly concentrated ionic liquid electrolytes. *ACS Appl. Mater. Interfaces* **14**, 13196–13205 (2022).
47. Yu, D., Zanelotti, C. J., Fox, R. J., Dingemans, T. J. & Madsen, L. A. Solvent-cast solid electrolyte membranes based on a charged rigid-rod polymer and ionic liquids. *ACS Appl. Energy Mater.* **4**, 6599–6605 (2021).
48. Dong, Q. et al. Insights into the dual role of lithium difluoro(oxalato)borate additive in improving the electrochemical performance of NMC811||graphite cells. *ACS Appl. Energy Mater.* **3**, 695–704 (2020).
49. Gao, H., Maglia, F., Lamp, P., Amine, K. & Chen, Z. Mechanistic study of electrolyte additives to stabilize high-voltage cathode-electrolyte interface in lithium-ion batteries. *ACS Appl. Mater. Interfaces* **9**, 44542–44549 (2017).
50. Swiderska-Mocek, A. & Gabryelczyk, A. Interfacial stabilizing effect of lithium borates and pyrrolidinium ionic liquid in gel polymer electrolytes for lithium-metal batteries. *J. Phys. Chem. C* **127**, 18875–18890 (2023).
51. Yu, X. et al. Direct observation of the redistribution of sulfur and polysulfides in Li-S batteries during first cycle by in situ X-ray fluorescence microscopy. *Adv. Energy Mater.* **5**, 1500072 (2015).
52. Freiberg, A. T. S. et al. Species in lithium-sulfur batteries using spatially resolved operando X-ray absorption spectroscopy and X-ray fluorescence mapping. *J. Phys. Chem. C* **122**, 5303–5316 (2018).
53. Sun, B. et al. At the polymer electrolyte interfaces: the role of the polymer host in interphase layer formation in Li-batteries. *J. Mater. Chem. A* **3**, 13994–14000 (2015).
54. Vairavamurthy, A. Using X-ray absorption to probe sulfur oxidation states in complex molecules. *Spectrochim. Acta A* **54**, 2009–2017 (1998).
55. Lin, Z. et al. High-performance lithium/sulfur cells with a bi-functionally immobilized sulfur cathode. *Nano Energy* **9**, 408–416 (2014).
56. Pickering, I. J., Prince, R. C., Divers, T. & George, G. N. Sulfur K-edge X-ray absorption spectroscopy for determining the chemical speciation of sulfur in biological systems. *FEBS Lett.* **441**, 11–14 (1998).
57. Dey, A. et al. Sulfur K-edge XAS and DFT calculations on nitrile hydratase: geometric and electronic structure of the non-heme iron active site. *J. Am. Chem. Soc.* **128**, 533–541 (2006).
58. Dezarnaud, C., Tronc, M. & Hitchcock, A. P. Inner shell spectroscopy of the carbon—sulfur bond. *Chem. Phys.* **142**, 455–462 (1990).
59. Jalilehvand, F. Sulfur: not a "silent" element any more. *Chem. Soc. Rev.* **35**, 1256–1268 (2006).

[1]Department of Chemistry, Virginia Tech, Blacksburg, VA, USA. [2]National Synchrotron Light Source II, Brookhaven National Laboratory, Upton, NY, USA. [3]Macromolecules Innovation Institute, Virginia Tech, Blacksburg, VA, USA. [4]Department of Materials Science and Engineering, Boise State University, Boise, ID, USA. [5]Department of Mechanical Engineering, Virginia Tech, Blacksburg, VA, USA. [6]Department of Materials Science and Engineering, University of Pennsylvania, Philadelphia, PA, USA. [7]Department of Materials Science and Engineering, Virginia Tech, Blacksburg, VA, USA. [8]Present address: Department of Materials Science and Engineering, Yonsei University, Seoul, South Korea. [9]These authors contributed equally: Jungki Min, Seong-Min Bak. ✉e-mail: fenglin@vt.edu

Methods

Materials

$LiNi_{0.8}Mn_{0.1}Co_{0.1}O_2$ (NMC811, average size of secondary particle = ~5 µm, primary particle size (200–500 nm), polycrystalline, CAMP) is provided by the Cell Analysis, Modeling, and Prototyping (CAMP) Facility in Argonne National Lab. Lithium poly(2,2′-disulfonyl-4,4′-benzidine terephthalamide) (LiPBDT, BlueSky Polymers) is used as received[1,2]. Sulfur (S_8, 99.98% trace metal basis), lithium difluoro(oxalate)borate (LiDFOB, purity ≥99.9%), *N*-methyl-2-pyrrolidone (NMP, anhydrous, 99.5%), PVDF-HFP (weight-average molecular weight (MW) ~455,000) and lithium bis(trifluoromethanesulfonyl)imide (LiTFSI, 99.99% trace metal basis, H_2O <250 ppm) are purchased from Sigma-Aldrich. 1-Butyl-1-methylpyrrolidinium bis(trifluoromethylsulfonyl) imide ($Pyr_{14}TFSI$, H_2O 83 ppm, 99.5%) IL is purchased from Iolitec. *N*-Methyl-*N*-propylpiperidinium bis(trifluoromethane sulfonyl)imide ($PP_{13}TFSI$) (H_2O <100 ppm, 99%) is purchased from Lanzhou Greenchem ILs. Li metal foils (purity ≥99.9%, thickness 0.2 mm) are purchased from China Energy Lithium. Carboxymethyl cellulose (CMC, purity ≥99.5%, mesh size 200, >85%) is purchased from MTI. Dimethylformamide (DMF, purity 99.7%, HPLC grade) and water (HPLC grade, pH 7) are purchased from Fisher Scientific. Polyvinylidene fluoride (PVDF, purity ≥99%) is purchased from MSE Supplies, and acetylene carbon black (purity ≥99.8%, particle size 35–40 nm) is purchased from MSE Supplies.

MIC membrane preparation

The basic MIC electrolyte is prepared at the benchtop (under ambient air condition) by dissolving 120 mg of LiPBDT in 12 g of H_2O (HPLC grade, pH 7, resistivity >18 MΩ cm at 25 °C, Fisher Scientific). LiTFSI (120 mg) and $Pyr_{14}TFSI$ (960 mg) are dissolved in 12 g of DMF ('MIC with additive' is prepared by the further addition of 60 mg LiDFOB). The solution is prepared at the benchtop under an ambient air environment. The chemicals (LiTFSI, $Pyr_{14}TFSI$ and DMF) are used as received. LiTFSI and $Pyr_{14}TFSI$ were stored in an Ar-filled glove box. After heating the two separate solutions in vials (6 Dram glass vial with screw-top closures, Fisher Scientific) to 80 °C inside an oven (Isotemp vacuum oven model 280A, Fisher Scientific) overnight under ambient air conditions, they were mixed by pouring into a glass vial with a screw cap (Fisher Scientific, 6 Dram vials, class B borosilicate glass) manually and equilibrated at 80 °C over another night[3]. The mixed solution is manually cast under ambient air on a 10 × 10 cm^2 glass plate and dried overnight at 80 °C in the oven (Isotemp vacuum oven model 280A, Fisher Scientific) under ambient air to evaporate the solvents. The MIC membrane is further dried at 100 °C in a vacuum oven under vacuum (applied pressure 27″Hg (inches mercury), Isotemp vacuum oven model 280A, Fisher Scientific) for 2 days. The MIC membrane is peeled off the glass substrate using a cutter blade (18 mm, Bazik Products) and punched into 19 mm disks using a precision disk cutter (MSK-T10, MTI) with ~100 µm thickness (measuring force <1.5 nN, digital thickness gauge, 547-526S, Mitutoyo).

Gel polymer electrolyte (GPE) membrane preparation

The general type of PE using poly(vinylidene fluoride-co-hexafluoropropylene) (PVDF-HFP) is prepared in a conventional lab for electrochemical cycling and X-ray synchrotron measurements. The GPE membrane is composed of PVDF-HFP (20 wt%), LiTFSI (20 wt%) and $PP_{13}TFSI$ (60 wt%)[4]. The GPE is prepared using PVDF-HFP (MW ~455,000, Sigma-Aldrich) as the polymer host, lithium bis(trifluoromethane sulfonyl)imide (LiTFSI, 99.99% trace metal basis, Sigma-Aldrich) and *N*-methyl-*N*-propylpiperidinium bis(trifluoromethane sulfonyl)imide ($PP_{13}TFSI$) IL (99%, Lanzhou Greenchem ILs). PVDF-HFP (160 mg) is dissolved in 120 mg of NMP (anhydrous, 99.5%) using a glass vial (Fisher Scientific, 6 Dram vials, class B borosilicate glass) and a magnetic stir bar (VWR) on a stir plate (11-100-16SH, Fisher Scientific) at 23 °C. $PP_{13}TFSI$ (480 mg) and LiTFSI (160 mg) were added to the mixture and mixed for 40 min at 23 °C. The slurry was cast on a glass plate and dried in a vacuum oven (Isotemp vacuum oven model 280A, Fisher Scientific) under vacuum (applied pressure 27″Hg) for 24 h at 80 °C. The GPE membrane is peeled off the glass substrate using a cutter blade (18 mm, Bazik Products) and punched into 19 mm disks using a precision disk cutter (MSK-T10, MTI) with ~230 µm thickness (measuring force <1.5 nN, digital thickness gauge, 547-526S, Mitutoyo).

Electrochemical characterizations

Cell assembly and testing. The positive electrode is prepared using 92% NMC811 active material, 4% PVDF binder and 4% acetylene carbon black in NMP. The slurry is prepared by adding 1 ml of NMP per 900 mg of combined solid components using a SpeedMixer (DAC 150.1 FVZ-K, Hauschild) under ambient air and cast onto carbon-coated aluminium foil (1 µm carbon double-sided coating on 15 µm aluminium foil, Canrd) current collector by doctor blade (BYK) under ambient air. The prepared slurry-coated electrode foil is punched into 10 mm diameter disks and dried overnight in a vacuum oven at 120 °C. The mass loading of the positive electrodes (averaged thickness of 60 µm) is 3.5 ± 0.5 mg cm^{-2}. For cross-sectional samples for synchrotron measurement, positive electrodes with an average mass loading of ~12 mg cm^{-2} were used for obtaining good quality XRF images. The Li|MIC|NMC811 coin cells and lithium symmetric coin cells were assembled in an argon-filled glove box with H_2O and O_2 level ≤0.1 ppm. The 0.2 MPa is applied to the coin cells and is assembled using Li metal electrodes with 15.6 mm diameter and 200 µm thickness. Electrochemical testing was performed using a Neware battery testing system (CT-4008T) inside a temperature-controlled testing chamber (DZF-6020, MTI). Three cells are tested for a single electrochemical experiment, and one of the cells is reported. The mass of the specific current and specific capacity refers to the mass of the active material in the positive electrode. The critical current density of the lithium symmetric cell is quantified by incremental current density steps at 23 °C and 60 °C. Li|MIC|NMC811 cells were cycled between 2.8 V and 4.4 V at 60 °C, except where indicated.

Measurement of transference number (t_+). Potentiostatic polarization measurements are carried out using a BioLogic SP-200 instrument with a lithium symmetric coin cell under a constant d.c. potential bias (ΔV = 10 mV) at 23 °C (rested the coin cell for 3 h at the OCP before carrying out the impedance measurement). The electrochemical impedance spectroscopy measurements are performed before and after the polarization in the frequency range of 5 MHz to 1×10^{-1} Hz at 23 °C. Data are collected with 100 points per decade, and the measurement is conducted using OCP time applied before carrying out experiments. The lithium-ion transference number was calculated using the following equation[5]:

$$t_+ = \frac{I_{ss}(\Delta V - I_0 R_0)}{I_0(\Delta V - I_{ss} R_{ss})}$$

where I_0 is the initial state current and I_{ss} is the steady-state current after 1 h. The R_0 refers to the initial cell impedance and R_{ss} is the steady-state cell impedance measured by electrochemical impedance spectroscopy.

Ionic conductivity measurement. Stainless steel (15.8 mm diameter with 1 mm thickness, 304 stainless steel, Canrd) symmetric coin cells are assembled (0.2 MPa) inside an Ar-filled glove box (H_2O <0.5 ppm, O_2 <0.5 ppm), sandwiching the basic MIC membrane with a thickness of 100 µm. The 'MIC with additive' membrane thickness is 250 µm. The diameter of stainless steel is 16 mm. The cells are rested at OCP overnight at 60 °C. Here the frequency range is 1 Hz to 1 MHz and collected with 100 points per decade under potentiostatic mode. The ionic conductivity is calculated using the following equation:

$$\sigma = \frac{d}{R_b \times S}$$

where d is the thickness of the MIC membrane, R_b is the bulk resistance (extrapolated from the intercept of the raw data at high frequency with the x-axis in the Nyquist plots) and S is the surface area of the stainless steel.

Physicochemical characterization

The cross-sectional Li|MIC|NMC811 sample, pristine and cycled MIC membrane morphology are characterized using a scanning electron microscope (FESEM, LEO 1550) and high-resolution transmission electron microscopy (HRTEM, JEOL JEM 2100). The chemical properties of the cycled MIC are quantitatively characterized by XPS (PHI VersaProbe III) using a monochromatic Al K-alpha X-ray source (1,486.6 eV) with a sputter rate of 7.7 nm min^{-1} for Ar sputtering.

Sample preparation for synchrotron measurements. The reference sulfur pellet (elemental sulfur, S_8) for energy shift correction in synchrotron measurements is prepared as follows. Sulfur powder (10 mg) is mixed with 90 mg of CMC binder and pressed into φ10 mm pellets by a pellet press (MTI Model YLJ-15). One side of the sulfur pellet is covered by Kapton tape (MYJOR) and the other side with Mylar film (3520 POLYPROPYLENE-THIN FILM for XRF, SPEX Sample Prep). The cross-sectional sample is prepared inside a glove box (H_2O <0.5 ppm, O_2 <0.5 ppm) and loaded onto a homemade sample holder (sealed in the aluminium pouch bag before taking out from an Ar-filled glove box), and then transferred into an He-filled measurement chamber (the samples are exposed to air less than 5 s during the transfer process when the Ar-filled aluminium pouch bag is opened). To prepare cross-sectional samples, cycled coin cells are transferred into an Ar-filled glove box (H_2O <0.5 ppm, O_2 <0.5 ppm) and disassembled by a coin cell crimper (MSK-160E, MTI) inside the Ar-filled glove box. Li|MIC|NMC811 components are carefully collected from the disassembled coin cell using stainless steel tweezers (AVEN) without any dislocation of each component and are sandwiched with Kapton tape (MYJOR). The Kapton tape sandwiched Li|MIC|NMC811 sample is prepared inside the Ar-filled glove box (H_2O <0.5 ppm, O_2 <0.5 ppm). The cross-sectional sample is carefully prepared by cutting the centre of the Kapton-sandwiched sample with a surgical knife (DEXSUR) from the Li metal side of the Li|MIC|NMC811 sample. Once the cross-sectional samples were carefully loaded onto the homemade sample holder, they were sealed in an aluminium pouch bag before being transferred from an Ar-filled glove box. The as-prepared Ar-filled aluminium pouch bag is used to transport samples from the Ar-filled glove box to the measurement chamber at the beamline. There was brief (less than 5 s) air exposure while placing the measurement station into the He-filled chamber at TES (8-BM) beamline of National Synchrotron Light Source II at Brookhaven National Laboratory.

Spatially resolved XRF/XAS measurement. The combined XRF imaging and XAS is performed by synchrotron X-rays in a fluorescence mode at the TES (8-BM) beamline of National Synchrotron Light Source II at Brookhaven National Laboratory. The beamline is optimized for tender energy X-ray at 2–5.5 keV using an Si (111) double-crystal monochromator with 5–20 µm tunable beam size. The incident X-ray beam energy is set at 2,500 eV, which is above the absorption edge of the sulfur. The measurement was conducted in the He-filled chamber at the TES beamline. There was air exposure (less than 5 s) while stationing the homemade sample holder into the He-filled measurement chamber. XRF image data are processed by PyXRF programme[6], and XAS data are analysed with the Demeter software package[7].

Topographical scanning and modulus measurement. Electrochemical AFM and nanoindentation measurements on pristine samples were performed using a Dimension Icon AFM (Bruker Nano) in ambient air condition, while measurements on cycled samples were performed on an identical system in an argon-filled glove box with both H_2O and O_2 concentration less than 0.1 ppm. The AFMs are controlled by Nanoscope V controllers and Nanoscope 9.4 software. Samples were fastened to a stainless steel puck (316 stainless steel, 14 mm diameter) by epoxy and then washed with dimethyl carbonate (99%, H_2O 20 ppm, Alfa Aesar). Topographic scanning was carried out in PeakForce Tapping mode using an Etalon HA_C (K-TEK Nanotechnology) probe with a nominal tip radius of 10 nm and a spring constant of 0.65 nm. Images took place over a 10 × 10 µm scan area with 1,024 × 1,024 pixel resolution at 0.25 Hz with PeakForce Setpoint 7.0 nN. Nanoindentation was conducted with a TAP150A probe (Bruker Nano) with a tip radius of 24.3 nm measured by a Ti roughness standard, a deflection sensitivity of 60.45 nm V^{-1} calibrated by ramping on sapphire and a spring constant of 4.93 N m^{-1} by the thermal tune method after obtaining the deflection sensitivity. During the nanoindentation process, 100 ramps were taken from 200 nm height at 0.25 Hz in a 10 × 10 grid with 1 µm separation between points. The trigger threshold chosen was 12 nN. AFM images were processed in NanoScope Analysis 2.0 (Bruker Nano), with some additional AFM image processing in ImageJ[8] (NIH). Nanoindentation force curves were processed in AtomicJ[9] using the classical focused grid, with further fine-tuning of the contact points by hand.

NMR diffusometry measurements. The MIC films were inserted into 5 mm diameter NMR sample tubes and dried at 100 °C under vacuum in a hot sand bath. The tubes were flame-sealed under vacuum before measuring diffusion. The NMR spectra and diffusion data were obtained using a Bruker Avance III 400 MHz/9.4 T wide-bore spectrometer equipped with a high gradient diffusion probe (Bruker Diff50) paired with a 5 mm ^{1}H RF coil insert. The NMR diffusometry experiments were performed over the temperature range of 25–80 °C with ≥5 min of thermal equilibration before acquiring data at each temperature. The pulsed-gradient stimulated echo experiment was run on ^{1}H and ^{19}F nuclei to obtain the self-diffusion coefficients of the cation and anion, respectively. The Stejskal–Tanner equation was used to fit the measured signal amplitude (I) as a function of gradient strength (g):

$$I = I_0 \exp\left(-D\gamma^2 g^2 \delta^2 \left(\Delta - \frac{\delta}{3}\right)\right)$$

where I_0 is the signal amplitude at $g = 0$, γ is the gyromagnetic ratio of the measured nucleus, δ is the effective (rectangular) gradient pulse duration, Δ is the diffusion time between gradient pulses and D is the self-diffusion coefficient. The measurements used a 90° pulse time of 3.7 µs for ^{1}H and 6 µs for ^{19}F, and an acquisition time of 0.02 s for both nuclei. The diffusion experiments used repetition times of 1–2 s, δ = 1 ms, Δ = 50 ms and max gradient strength ranging from 600 G cm^{-1} to 1,500 G cm^{-1} to achieve ≥85% signal attenuation in 16 steps.

XPS. The binding energy scale was calibrated from the aliphatic hydrocarbon C 1s peak at 284.8 eV for XPS measurements. The cycled Li|MIC|NMC811 cells are disassembled inside the Ar-filled glove box (H_2O <0.5 ppm, O_2 <0.5 ppm). The MIC membrane is collected with a stainless steel tweezer (AVEN) and gently rinsed with 0.1 ml of dimethyl carbonate (≥99.9%, H_2O <10 ppm, Sigma-Aldrich) to remove excess IL covering the surface, and then dried inside the Ar-filled glove box (H_2O <0.5 ppm, O_2 <0.5 ppm) for several minutes before mounting on the XPS sample stud. Two sides of the MIC membrane are loaded on the sample holder with double-sided adhesive tape and sealed in a transfer vessel with argon. The transfer vessel was then docked onto the XPS instrument without air exposure. XPS measurements were carried out at the Surface Analysis Laboratory of the Chemistry Department at Virginia Tech.

XPS was performed using a PHI VersaProbe III instrument (Physical Electronics) using a monochromatic Al K X-ray source operated at 50 W (1,486.6 eV) with the analysis area of 1,000 × 200 µm^2. Depth profiling experiments were conducted on the sample surface using an Ar ion beam gun with an etching rate of 7.7 nm min^{-1} (calibrated by SiO_2).

Peak fittings and quantification were done using PHI MultiPak software version 9.9.0.8. A Shirley background and Gauss–Lorentz peak shape were applied to fitted peaks. The software provided corrected sensitivity factors for quantification.

High-performance liquid chromatography combined with ultraviolet spectroscopy (HPLC-UV). The separation and detection of impurities were conducted using an Agilent 1200 HPLC system. The system included a quaternary pump (1311A), an autosampler (1329B), an oven heater (1316A) and a UV diode array detector. A Phenomenex LUNA C18 column (250 × 4.6, 5 µm) was utilized for the separation process.

For the analysis, we used an isocratic mobile phase consisting of 90% aqueous solution with 0.1% trifluoroacetic acid (TFA, ≥99.5%, Fisher Scientific) and 10% acetonitrile (CH_3CN, 99.9%, Fisher Scientific) with 0.1% TFA. Gradient elution was used for separation, starting at 90/10% at time 0 and ending at 10/90% over 10 min, followed by a hold at 10/90% for an additional 2 min. The deuterated chloroform eluent (chloroform-D (99.8%) + 0.05% (v/v) TMS, Cambridge Isotope Laboratories) containing by-product is evaporated and added with the solution of mobile phase (90% aqueous solution with 0.1% TFA and 10% acetonitrile (CH_3CN) with 0.1% TFA). The injection volume was set to 20 µl, and the flow rate was maintained at 1 ml min^{-1}. Detection was performed at 254 nm and 280 nm wavelengths.

Synchrotron X-ray micro-computed tomography. The micro-computed tomography scans were conducted at the beamline 2-BM of the Advanced Photon Source, Argonne National Laboratory. The X-ray beam energy used was 30.0 keV, and each tomography scan was collected within 360° rotation, consisting of 3,000 projections, an angle step of 0.12° and a 0.06 s exposure time; therefore, each scan took 180 s. With a camera pixel size of 3.45 µm and a lens magnification of 7.5×, the ideal imaging resolution is 0.46 µm per pixel. However, with the limitation of the detector, binned projections were collected, resulting in a resolution of 0.92 µm per pixel and projection size of 3,232 × 2,426 pixels (corresponding to a field view of ~2.97 mm in width and ~2.23 in height). To prepare tomography samples, a cycled coin cell (Li|MIC|NMC811 after 200th cycles, 2.8–4.4 V, 67 mA g^{-1} and 60 °C) is transferred into the Ar-filled glove box (H_2O <0.5 ppm, O_2 <0.5 ppm) and disassembled by a coin cell crimper (MSK-160E, MTI) inside the Ar-filled glove box. The cycled MIC membrane (after 200th cycles, 2.8–4.4 V, 67 mA g^{-1} and 60 °C) is carefully collected from the Li|MIC|NMC811 cell using stainless steel tweezers (AVEN) inside the Ar-filled glove box (H_2O <0.5 ppm, O_2 <0.5 ppm). The cycled MIC membrane and pristine MIC membrane are separately sealed in a glass vial with caps (Fisher Scientific, 6 Dram vials, class B borosilicate glass) and labelled, and then wrapped with parafilm (laboratory film PM-996, Amcor) inside the Ar-filled glove box (H_2O <0.5 ppm, O_2 <0.5 ppm). Then, samples are sealed in aluminium pouch bags inside the Ar-filled glove box (H_2O <0.5 ppm, O_2 <0.5 ppm), transferred out and shipped for tomography measurements. The MIC films were cut into strips and put into Kapton tubes (transparent under X-ray) with a diameter of 1.5 mm. The tomographic reconstructions were performed using TomoPy[10], analysed using ImageJ and rendered with Avizo (Thermo Fisher Scientific). To show whether there are internal porosities in the MIC films, the rendered volumes were set in transparent mode for three-dimensional visualization.

Data availability

The data supporting the findings of this study are available in the published article and its Supplementary Information. Source data are provided with this paper.

Acknowledgements

This work was primarily supported by the US Department of Energy's Office of Energy Efficiency and Renewable Energy (EERE) under award number DE-EE0008860 (F.L. and L.A.M.). Part of the work was also supported by the Assistant Secretary for Energy Efficiency and Renewable Energy, Office of Vehicle Technologies of the US Department of Energy through the Advanced Battery Materials Research (BMR) Program (Battery500 Consortium) under contract number 683639 (F.L. and L.A.M.). F.L. and L.A.M. also acknowledge the seedling support from the Virginia Tech College of Science Strategic Initiative in Energy (03400). This work used shared facilities at the Virginia Tech Nanoscale Characterization and Fabrication Laboratory (NCFL) and Surface Analysis Laboratory, supported by the National Science Foundation (NSF) under grant number CHE-1531834. This research used 8-BM of the National Synchrotron Light Source II (NSLS-II), which is a US Department of Energy Office of Science User Facility at Brookhaven National Laboratory under contract number DE-SC0012704. This research used resources of the Advanced Photon Source, a US Department of Energy (DOE) Office of Science User Facility operated for the DOE Office of Science by Argonne National Laboratory under contract number DE-AC02-06CH11357. NMC811 was produced at the US Department of Energy's (DOE) CAMP (Cell Analysis, Modeling, and Prototyping) Facility, Argonne National Laboratory. The CAMP Facility is fully supported by the DOE Vehicle Technologies Program (VTP) within the core funding of the Applied Battery Research (ABR) for Transportation Program. We thank M. Hedge and T. J. Dingemans (University of North Carolina-Chapel Hill) and D. Yu (Virginia Tech) for discussions. We also thank M. Ashraf-Khorasani for chromatography analysis and discussions.

Author contributions

F.L. conceived and led the project. F.L. and J.M. designed the experiments. J.M. performed the materials synthesis, electrochemical measurements and characterizations. J.M., S.-M.B. and Y.D. performed the synchrotron X-ray characterization. Y.Z. and M.Y. assisted with the membrane processing. D.X. and L.T. helped with data analysis. J.A.R. and H.X. conducted ex situ atomic force microscopy. N.F.P. and L.A.M. conducted the pulsed-field-gradient NMR diffusiometry and participated in scientific discussions. Z.D. and L.L. conducted synchrotron X-ray micro-computed tomography. J.M. and F.L. analysed all the data and wrote the paper with the assistance of L.A.M. and S.-M.B. All authors approved the paper for publication.

Competing interests

Part of the results in this paper is included in a patent application (application no. 63/734,312) filed by some co-authors (J.M., L.A.M. and F.L.).

Additional information

Extended data is available for this paper at https://doi.org/10.1038/s41565-025-01885-5.

Supplementary information The online version contains supplementary material available at https://doi.org/10.1038/s41565-025-01885-5.

Correspondence and requests for materials should be addressed to Feng Lin.

Peer review information *Nature Nanotechnology* thanks Xin Guo and the other, anonymous, reviewer(s) for their contribution to the peer review of this work.

https://doi.org/10.1038/s41565-025-01885-5

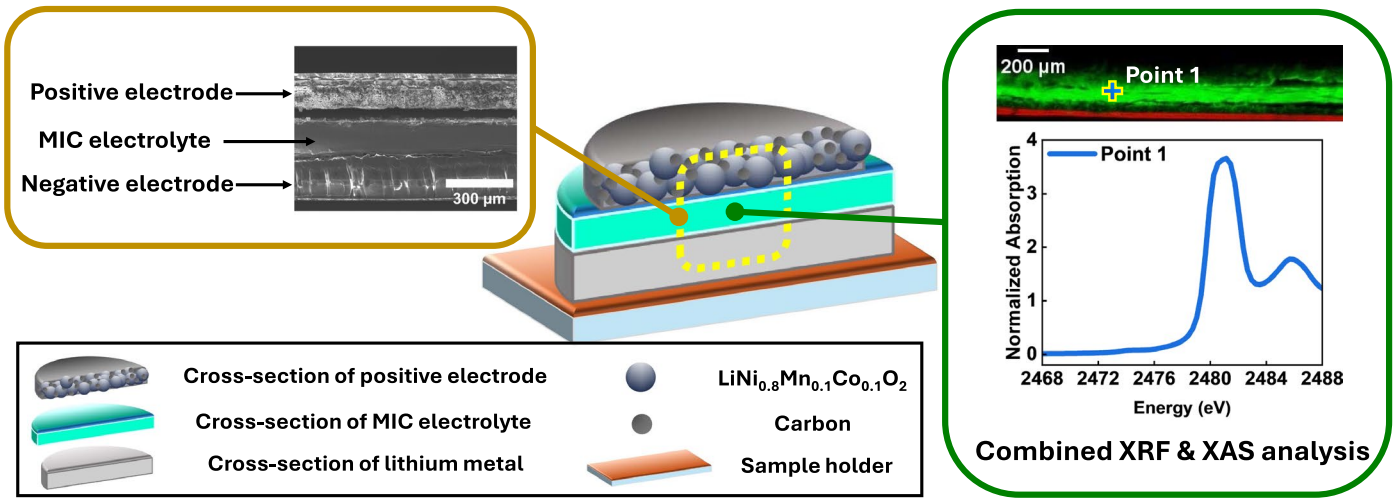

Extended Data Fig. 1 | Graphic representation of synchrotron X-ray measurements to investigate interfacial degradation in polymer electrolyte-based cells. Schematic showing synchrotron X-ray measurements of a solid-state battery cross-section, which combines X-ray fluorescence (XRF) microscopy and X-ray absorption spectroscopy (XAS) measurements to visualize ionic concentration and probe chemical states across buried interfaces of solid-state battery components. Sulfur species from IL ($TFSI^-$) and PBDT polymer ($-SO_3^-$) are present in the MIC electrolyte. Tracking the sulfur species of polymer electrolytes with XRF mapping reveals local ionic concentration heterogeneities, and spatially resolved XAS analysis informs the evolution of new sulfur species from interfacial side reactions by probing the changes in the oxidation states of sulfur elements therein. From the right panel of the XRF map, the green area represents the regions containing sulfur species, the black areas indicate regions without sulfur species, and the red area represents the sample holder (see also **Spatially resolved XRF/XAS measurement** and **Sample preparation for synchrotron measurements** from **Methods**). The point scanning XAS on the cross-sectional sample probes sulfur chemical states across electrode|electrolyte interfaces with a spatial resolution of a few micrometers (Right part, point 1).